Available online at www.sciencedirect.com
SCIENCE DIRECT®
International Journal of Heat and Mass Transfer 49 (2006) 2254–2264
International Journal of HEAT and MASS TRANSFER
www.elsevier.com/locate/ijhmt

Three-dimensional modeling of heat transfer and fluid flow in laminar-plasma material re-melting processing

Hai-Xing Wang [a], Kai Cheng [a], Xi Chen [a,*], Wenxia Pan [b]

[a] Department of Engineering Mechanics, Engineering Thermophysics Division, Tsinghua University, Beijing 100084, China
[b] Institute of Mechanics, Chinese Academy of Sciences, Beijing 100080, China

Received 18 July 2005; received in revised form 2 November 2005
Available online 20 February 2006

Abstract

Modeling study is performed concerning the heat transfer and fluid flow for a laminar argon plasma jet impinging normally upon a flat workpiece exposed to the ambient air. The diffusion of the air into the plasma jet is handled by using the combined-diffusion-coefficient approach. The heat flux density and jet shear stress distributions at the workpiece surface obtained from the plasma jet modeling are then used to study the re-melting process of a carbon steel workpiece. Besides the heat conduction within the workpiece, the effects of the plasma-jet inlet parameters (temperature and velocity), workpiece moving speed, Marangoni convection, natural convection etc. on the re-melting process are considered. The modeling results demonstrate that the shapes and sizes of the molten pool in the workpiece are influenced appreciably by the plasma-jet inlet parameters, workpiece moving speed and Marangoni convection. The jet shear stress manifests its effect at higher plasma-jet inlet velocities, while the natural convection effect can be ignored. The modeling results of the molten pool sizes agree reasonably with available experimental data.

Keywords: Plasma-jet heating; Metal re-melting; Molten-pool flow and heat transfer; Three-dimensional modeling

1. Introduction

Stable and silent long laminar plasma jets have been successfully generated at the atmospheric pressure in recent years with elaborately designed DC arc plasma torches [1,2]. Since only molecular diffusion mechanism is involved in the laminar plasma jet, the entrainment of the ambient air into the laminar plasma jet is significantly reduced. The length of the high-temperature region in the laminar plasma jet is therefore much longer than that in the conventional turbulent plasma jet, leading to much smaller axial gradients of plasma temperature, axial velocity and species concentration in the laminar plasma jet. Furthermore, the length of the laminar plasma jet can be easily adjusted by changing the arc current and/or the working-gas flow rate of the plasma torch used for generating the laminar plasma jet [2]. These merits inherent in the long laminar plasma jet make it attractive from the viewpoint of materials processing, since it provides a new possibility to achieve low-noise working surroundings, better process repeatability and controllability, and reduced oxidation degree of metallic materials processed in air surroundings. The preliminary attempts [2–4] that use the laminar plasma jet in the preparation of thermal barrier coatings, in the re-melting hardening of cast iron and other metals and in the stainless-steel surface cladding, have shown rather encouraging results such as the fine microstructure, low surface roughness and small porosity of the prepared coatings, the good re-melting process controllability and surface morphologies, as well as the preferable metallurgically bonded clad layer.

The schematic of the laminar plasma jet re-melting hardening of metal surface is shown in Fig. 1 [3]. The plasma jet impinges normally upon the workpiece moving in the direction perpendicular to the plasma jet axis. With the laminar

* Corresponding author. Tel.: +86 10 6278 4127; fax: +86 10 6278 1824.
E-mail address: cx-dem@mail.tsinghua.edu.cn (X. Chen).

0017-9310/$ - see front matter © 2006 Elsevier Ltd. All rights reserved.
doi:10.1016/j.ijheatmasstransfer.2005.11.019

Nomenclature

c_p	specific heat at constant pressure (J kg^{-1} K^{-1})
$\overline{D}^{x}_{AB}$	combined ordinary diffusion coefficient (m^2 s^{-1})
$\overline{D}^{T}_{AB}$	combined thermal diffusion coefficient (kg m^{-1} s^{-1})
f	liquid-phase fraction
f_A	argon mass fraction in argon–air mixture
g	gravity acceleration (m s^{-2})
h	specific enthalpy (J kg^{-1}); workpiece thickness (m)
J	diffusion mass flux vector (kg m^{-2} s^{-1})
L	latent heat (J kg^{-1})
m	particle mass (kg)
$\overline{m}$	average mass of all the heavy particles (excluding electrons) (kg)
$\overline{M}$	average mass of all the gas particles (including electrons) (kg)
n	gas particle number density (m^{-3})
p	pressure (Pa)
q	heat flux density (W m^{-2})
R	plasma jet-inlet radius (m)
r, z	radial and axial coordinates (m)
S	source term
T	temperature (K)
T_0	highest temperature at jet-inlet center (K)
U_0	maximum axial-velocity at jet-inlet center (m s^{-1})
U_r	radiation power loss per unit volume of plasma (W m^{-3})
U_s	workpiece moving speed (m s^{-1})
u, v, w	x-, y- and z-velocity component (m s^{-1})
X_A	argon mole fraction
x, y, z	Cartesian coordinates

Greek symbols

β	volumetric expansion coefficient (K^{-1})
Γ_f	transport coefficient in mass conservation equation (kg m^{-1} s^{-1})
μ	viscosity (Pa s)
ρ	mass density (kg m^{-3})
σ	surface tension (N m^{-1})
τ	shear stress (N m^{-2})

Subscripts

0	jet inlet center
A	gas A (argon)
B	gas B (air)
f	about mass fraction

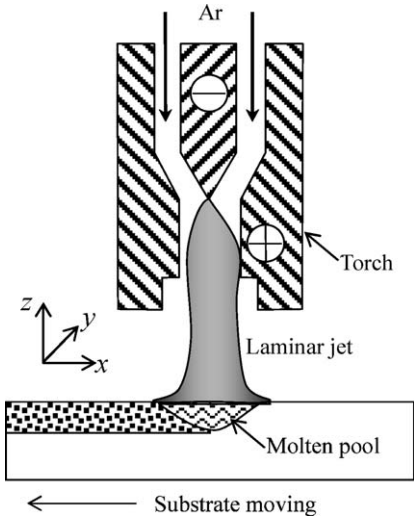

Fig. 1. Schematic of the plasma re-melting processing and coordinate system.

plasma jet re-melting hardening of cast iron and other metallic surfaces [3,4] as the main research background, a detailed modeling study is performed to consider the heat transfer and fluid flow in laminar-plasma material re-melting processing. Such modeling study is thus far not available, although many papers have been published about the modeling of heat transfer and fluid flow in plasma, arc, laser and electron-beam welding, melting and other materials processing [5]. Different approaches were used in those previous papers, from various pure heat conduction models (e.g. using a moving point, line or surface heat source method) to much more complex models considering the convection caused by the surface tension gradient, Lorentz force, buoyancy, jet impact pressure and shear stress, etc. The special feature of the laminar plasma-jet re-melting process discussed here is that there exists no Joule heating nor Lorentz force in the workpiece (unlike the plasma or arc welding [6,7]), but there exists the shear stress caused by the impinging plasma jet (unlike the laser welding or re-melting [8]).

In this paper, modeling study is first conducted concerning the heat transfer and fluid flow for a laminar argon plasma jet impinging normally upon a flat workpiece exposed to the ambient air. The diffusion of the ambient air into the plasma jet is handled by use of the combined-diffusion-coefficient method [9,10]. The distributions of the temperature, velocity and argon mass fraction in the plasma jet and the heat flux density, shear stress and impact pressure on the workpiece surface are obtained from the jet-region computation. Numerical simulation is then conducted using the computed heat flux density and shear stress distributions on the workpiece surface caused by the impinging laminar plasma jet as the boundary conditions to study the heat transfer and fluid flow in the re-melting processing of the metallic workpiece. Besides heat

conduction within the workpiece, the plasma-jet heat flux and shear stress, workpiece moving speed, Marangoni convection, natural convection etc. are also considered to examine their effects on the re-melting molten pool characteristics. It is expected that the workpiece motion in the direction perpendicular to the plasma-jet axis will cause three-dimensional (3-D) effect in the plasma-jet region. Such a 3-D effect can, however, be safely neglected in the plasma-jet region since the workpiece moving speed is always much less than the jet velocities (a few mm s^{-1} vs. 10^2 m s^{-1}). A 2-D modeling approach is thus justified for the plasma-jet region modeling. On the other hand, the effect of workpiece moving speed on molten pool shape and sizes in the workpiece cannot be ignored, and thus a 3-D modeling approach is employed to the workpiece re-melting process.

2. Modeling approach

2.1. Laminar plasma impinging-jet

The main assumptions used in the modeling study of the plasma jet include steady, laminar and axi-symmetrical flow with negligible swirling velocity component; local thermodynamic equilibrium (LTE) and optically thin plasma; diffusion of the ambient air into the plasma jet can be handled by the combined-diffusion-coefficient method [9–13]. The governing equations including the mass, momentum, energy, and gas species conservation equations in the cylindrical coordinate system are similar to those used in [11–13] and can be written as follows:

$$\frac{\partial}{\partial z}(\rho v_z)+\frac{1}{r}\frac{\partial}{\partial r}(r\rho v_r)=0 \tag{1}$$

$$\frac{\partial(\rho v_z v_z)}{\partial z}+\frac{1}{r}\frac{\partial(r\rho v_z v_r)}{\partial r} =-\frac{\partial p}{\partial z}+2\frac{\partial}{\partial z}\left[\mu\frac{\partial v_z}{\partial z}\right]+\frac{1}{r}\frac{\partial}{\partial r}\left[r\mu\left(\frac{\partial v_z}{\partial r}+\frac{\partial v_r}{\partial z}\right)\right] \tag{2}$$

$$\frac{\partial(\rho v_z v_r)}{\partial z}+\frac{1}{r}\frac{\partial(r\rho v_r v_r)}{\partial r} =-\frac{\partial p}{\partial r}+\frac{2}{r}\frac{\partial}{\partial r}\left[r\mu\frac{\partial v_r}{\partial r}\right]+\frac{\partial}{\partial z}\left[\mu\left(\frac{\partial v_r}{\partial z}+\frac{\partial v_z}{\partial r}\right)\right]-2\mu\frac{v_r}{r^2} \tag{3}$$

$$\begin{aligned}\frac{\partial(\rho v_z h)}{\partial z}+\frac{1}{r}\frac{\partial(r\rho v_r h)}{\partial r} &=\frac{\partial}{\partial z}\left[\frac{k}{c_p}\frac{\partial h}{\partial z}\right]+\frac{1}{r}\frac{\partial}{\partial r}\left[r\frac{k}{c_p}\frac{\partial h}{\partial r}\right]-U_r-\frac{\partial}{\partial z}[(h_A-h_B)J_z]\\ &\quad-\frac{1}{r}\frac{\partial}{\partial r}[r(h_A-h_B)J_r]-\frac{\partial}{\partial z}\left[\frac{k}{c_p}(h_A-h_B)\frac{\partial f_A}{\partial z}\right]\\ &\quad-\frac{1}{r}\frac{\partial}{\partial r}\left[r\frac{k}{c_p}(h_A-h_B)\frac{\partial f_A}{\partial r}\right]\end{aligned} \tag{4}$$

$$\frac{\partial(\rho v_z f_A)}{\partial z}+\frac{1}{r}\frac{\partial(r\rho v_r f_A)}{\partial r} =\frac{\partial}{\partial z}\left[\Gamma_f\frac{\partial f_A}{\partial z}\right]+\frac{1}{r}\frac{\partial}{\partial r}\left[r\Gamma_f\frac{\partial f_A}{\partial r}\right]+S_f \tag{5}$$

where v_z and v_r are the axial and radial velocity components, ρ, μ, k, c_p, h and U_r are the temperature- and composition-dependent plasma density, viscosity, thermal conductivity, specific heat at constant pressure, specific enthalpy and radiation power per unit volume of plasma, respectively, and p and f_A are gas pressure and argon mass fraction in the argon–air mixture. In Eq. (4), the terms containing $(h_A - h_B)$ represent the contribution of species diffusion to the energy transport, where h_A and h_B are the temperature-dependent specific enthalpies of gases A (argon) and B (air), respectively. J_z and J_r are the axial and radial components of the argon diffusion mass flux vector which can be expressed as $J_A = -(n^2/\rho)\overline{m}_A\overline{m}_B\overline{D}^x_{AB}\times\nabla X_A - \overline{D}^T_{AB}\nabla \ln T$, where n is the total gas-particle number density, $\overline{m}_A$ and $\overline{m}_B$ are the averaged particle masses for all the heavy gas particles (excluding electrons) coming from argon and those from air, X_A is the mole fraction of argon in the argon–air mixture, whereas $\overline{D}^x_{AB}$ and $\overline{D}^T_{AB}$ are the combined ordinary diffusion coefficient associated with the argon mole fraction gradient ∇X_A and the combined thermal diffusion coefficient associated with the temperature gradient ∇T, respectively [9]. The transport coefficient in Eq. (5) can be expressed by $\Gamma_f = [\overline{m}_A\overline{m}_B/(\overline{M}\overline{M}_A)]\rho\overline{D}^x_{AB}$ [11,12], in which $\overline{M}$ and $\overline{M}_A$ are the averaged gas-particle mass for all the gas particles (including electrons) of the gas mixture and that for all the gas particles coming from argon, respectively [9], whereas the source term S_f can be expressed as [11,12]

$$\begin{aligned}S_f &=\frac{\partial}{\partial z}\left(\Gamma_f\frac{f_A}{\overline{M}}\frac{\partial\overline{M}}{\partial z}\right)-\frac{\partial}{\partial z}\left(\Gamma_f\frac{f_A}{\overline{M}_A}\frac{\partial\overline{M}_A}{\partial z}\right)\\ &\quad+\frac{1}{r}\frac{\partial}{\partial r}\left(r\Gamma_f\frac{f_A}{\overline{M}}\frac{\partial\overline{M}}{\partial r}\right)-\frac{1}{r}\frac{\partial}{\partial r}\left(r\Gamma_f\frac{f_A}{\overline{M}_A}\frac{\partial\overline{M}_A}{\partial r}\right)\\ &\quad+\frac{\partial}{\partial z}\left(\overline{D}^T_{AB}\frac{\partial\ln T}{\partial z}\right)+\frac{1}{r}\frac{\partial}{\partial r}\left(r\overline{D}^T_{AB}\frac{\partial\ln T}{\partial r}\right)\end{aligned} \tag{6}$$

The computational domain employed in this study is the region A–G–H–I–A shown in Fig. 2, i.e. only the right semi-plane of the axi-symmetrical impinging jet region is included. The upper side of plane J–D–E is the plasma torch with A–B being the plasma flow inlet. B–C–D is a backward-step region, whereas J–D is the torch exit. I–H is the workpiece surface, whereas F–G and G–H are the free boundaries, respectively. In the computation, the radial size (AG) of the computational domain is set to be 50 mm, whereas axial size (AI) is 18 mm. Other sizes adopted are as follows: the radius of plasma jet inlet (AB) is 2 mm, torch exit inner radius (JD) 4 mm, torch-wall thickness (BF) 33 mm, backward-step length (CD) is 8 mm.

The boundary conditions used in the jet modeling include that at the jet inlet A–B, zero radial velocity, argon mass fraction $f_A = 1.0$ and the power-law profiles of temperature and axial velocity $T = (T_0 - T_w)[1 - (r/R)^{2.3}] + T_w$, $v_z = U_0[1 - (r/R)^{1.4}]$ are used [12,13], where T_w and R are torch wall temperature (700 K) and jet-inlet radius

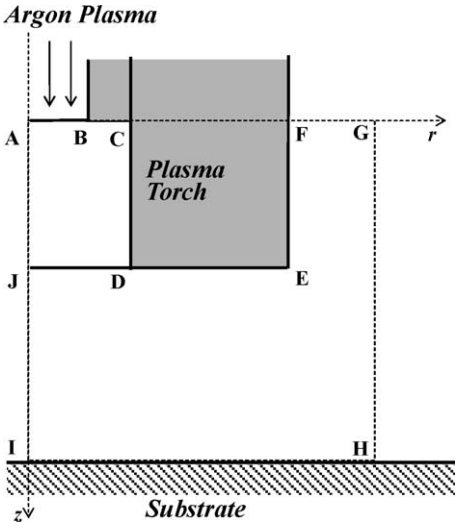

Fig. 2. Computational domain for the impinging laminar plasma jet modeling.

(2 mm). Axi-symmetrical conditions are employed along the jet axis A–I; free boundary conditions are employed along F–G and G–H; and zero velocity, fixed temperature and zero diffusion flux are used at the solid surfaces.

The SIMPLE algorithm and 92 (z-) × 187 (r-) grid points are employed in the computation with finer mesh spacing near the jet axis. The plasma properties are calculated from local values of plasma temperature (or specific enthalpy) and argon mass fraction using the property tables pre-compiled for different plasma temperatures (300–30,000 K with a spacing of 100 K) and different argon–air mass fraction ratios [10]. More calculation details about the plasma jet characteristics can be found in Refs. [11–13].

2.2. Heating of the workpiece by the plasma jet

The main assumptions employed in the workpiece heating study include that the re-melting process is steady in the coordinate system (x,y,z) fixed with respect to the plasma torch or plasma-jet axis and there is no deformation on the top surface of the molten pool (flat surface), as assumed in many previous studies [5–8]. Based on these assumptions, the governing equations in the Cartesian coordinate system (x,y,z) to describe the melt flow and heat transfer in the workpiece are as follows [8]:

$$\frac{\partial(\rho u)}{\partial x}+\frac{\partial(\rho v)}{\partial y}+\frac{\partial(\rho w)}{\partial z}=0 \tag{7}$$

$$\rho\left(u\frac{\partial u}{\partial x}+v\frac{\partial u}{\partial y}+w\frac{\partial u}{\partial z}\right) =\frac{\partial}{\partial x}\left[2\mu\left(\frac{\partial u}{\partial x}\right)\right]+\frac{\partial}{\partial y}\left[\mu\left(\frac{\partial u}{\partial y}+\frac{\partial v}{\partial x}\right)\right] +\frac{\partial}{\partial z}\left[\mu\left(\frac{\partial u}{\partial z}+\frac{\partial w}{\partial x}\right)\right]-\frac{\partial p}{\partial x}+S_u \tag{8}$$

$$\rho\left(u\frac{\partial v}{\partial x}+v\frac{\partial v}{\partial y}+w\frac{\partial v}{\partial z}\right) =\frac{\partial}{\partial x}\left[\mu\left(\frac{\partial v}{\partial x}+\frac{\partial u}{\partial y}\right)\right]+\frac{\partial}{\partial y}\left[2\mu\left(\frac{\partial v}{\partial y}\right)\right] +\frac{\partial}{\partial z}\left[\mu\left(\frac{\partial v}{\partial z}+\frac{\partial w}{\partial y}\right)\right]-\frac{\partial p}{\partial y}+S_v \tag{9}$$

$$\rho\left(u\frac{\partial w}{\partial x}+v\frac{\partial w}{\partial y}+w\frac{\partial w}{\partial z}\right) =\frac{\partial}{\partial x}\left[\mu\left(\frac{\partial w}{\partial x}+\frac{\partial u}{\partial z}\right)\right]+\frac{\partial}{\partial y}\left[\mu\left(\frac{\partial w}{\partial y}+\frac{\partial v}{\partial z}\right)\right] +\frac{\partial}{\partial z}\left[2\mu\left(\frac{\partial w}{\partial z}\right)\right]-\frac{\partial p}{\partial z}+S_w+S_b \tag{10}$$

$$\rho c\left(u\frac{\partial T}{\partial x}+v\frac{\partial T}{\partial y}+w\frac{\partial T}{\partial z}\right) =\frac{\partial}{\partial x}\left(k\frac{\partial T}{\partial x}\right)+\frac{\partial}{\partial y}\left(k\frac{\partial T}{\partial y}\right)+\frac{\partial}{\partial z}\left(k\frac{\partial T}{\partial z}\right)+S_{\mathrm{h}} \tag{11}$$

Here x is along the workpiece bottom-surface and in the direction opposite to the workpiece motion, y along the bottom surface but normal to x or the workpiece motion direction, whereas z is normal to the workpiece surface and directed to the plasma jet region. u, v and w are the x-, y- and z-velocity components, T and p the temperature and pressure, whereas now ρ, μ and k are the density, viscosity and thermal conductivity of the workpiece material, respectively. In order to account for the solid–liquid phase change in the workpiece, the fixed-grid method suggested by Voller et al. [14] is used. Namely, the heat and momentum transfer on the solid–liquid phase interface is incorporated into the governing equations through introducing suitable volume source terms. The source terms S_u, S_v and S_w introduced in the momentum equations (8)–(10) take the following forms [8]:

$$S_u=A(u+U_{\mathrm{s}}),\quad S_v=Av,\quad S_v=Aw, \tag{12}$$

where parameter A depends on the processed material and the local liquid-phase fraction f (f is in the range of $0\leqslant f\leqslant 1$), and $A=-C(1-f)^2/(f^3+q)$ for the materials with a phase-change mushy region, whereas q is merely a small constant introduced to avoid division by zero in the computation and C is a large constant (e.g. 10^{10}). U_{s} is the absolute value of workpiece moving velocity and thus $u=-U_{\mathrm{s}}$ is obtained in the solid-phase region with $f=0$. The local value of the liquid-phase fraction f in the workpiece is calculated from the local temperature and the solidus temperature (T_{S}) and liquidus temperature (T_{L}) of the melting mushy-region by use of the following relations:

$$f=0\quad \text{for } T\leqslant T_{\mathrm{S}}\quad \text{(solid-phase region)} \tag{13a}$$

$$f=\frac{T-T_{\mathrm{S}}}{T_{\mathrm{L}}-T_{\mathrm{S}}}\quad \text{for } T_{\mathrm{S}}<T<T_{\mathrm{L}}\quad \text{(mushy region)} \tag{13b}$$

$$f=1\quad \text{for}\quad T_{\mathrm{L}}\leqslant T\ \text{(liquid-phase region)} \tag{13c}$$

S_h in Eq. (11) is introduced to account for the latent heat release, and takes the following form [8]:

$$S_h = -\rho L\left(u\frac{\partial f}{\partial x} + v\frac{\partial f}{\partial y} + w\frac{\partial f}{\partial z}\right) \tag{14}$$

in which L is the melting latent-heat of processed material. The additional source term S_b in the momentum equation (10) in the z-(vertical) direction is introduced to account for the natural convection in the molten pool, and

$$S_b = f\rho g\beta(T - T_L) \tag{15}$$

where Boussinesq approximation has been used. In Eq. (15), β is the volume expansion coefficient, and g is the gravity acceleration.

Using this approach, the motion and heat transfer of both solid and liquid phases in the workpiece can be solved in a unified way [8,14] using the SIMPLE-like algorithm [15,16].

Boundary conditions employed in the study of workpiece heating are as follows: at the upstream (right side) boundary, $u = -U_s$, $v = 0$, $w = 0$ and $T = T_a$ (T_a is the ambient temperature). At the downstream (left side) boundary, $u = -U_s$, $v = 0$, $w = 0$ and $\partial T/\partial x = 0$. At the vertical symmetrical plane (x–z plane with $y = 0$): $\partial u/\partial y = 0$, $v = 0$, $\partial w/\partial y = 0$ and $\partial T/\partial y = 0$. At the bottom surface and lateral surfaces, $u = -U_s$, $v = 0$, $w = 0$ and $T = T_a$. At the top surface of molten pool with higher temperatures and non-uniform melt temperature distribution, the effects on melt flow and heat transfer of Marangoni convection (caused by the surface tension gradient), the shear stress produced by the impinging plasma jet and the radiation heat loss from top surface are considered. Hence, the following boundary conditions are employed at the top surface of workpiece:

$$\mu\frac{\partial u}{\partial z} = f\left(\frac{\partial\sigma}{\partial T}\frac{\partial T}{\partial x} + \tau_x\right), \qquad \mu\frac{\partial v}{\partial z} = f\left(\frac{\partial\sigma}{\partial T}\frac{\partial T}{\partial y} + \tau_y\right),$$

$$w = 0, \quad k(\partial T/\partial z) = q_j - \varepsilon\Sigma T^4 \tag{16}$$

Here τ_x and τ_y are the x- and y-components of the shear stress produced by the plasma jet at the workpiece surface; σ is the surface tension coefficient, ε and Σ are the emissivity and the Stefan–Boltzmann constant, whereas q_j is the local heat flux density from the plasma jet to the workpiece surface. Since the calculated highest temperatures on the molten pool are always lower than the boiling point of studied metal (carbon steel) as seen later on in this paper, the effect of metal vaporization on the heat flux at the top surface is not considered in Eq. (16).

The computation is actually performed for the cylindrical volume with sizes $0 \leqslant r \leqslant 15$ mm, $0 \leqslant \theta \leqslant \pi$ and $0 \leqslant z \leqslant 10$ mm using the non-commercial code FAST-3D [16]. Altogether 36 (r-direction) × 12 (θ-direction) × 36 (z-direction) grid points are employed in the workpiece re-melting modeling for most cases. In the computation, the averaged values of ϕ_i ($i = 1, 2, \ldots, N$) at all the N grid points in the θ-direction and on the small circle nearest to the axis in the mesh are employed [11] along the geometrical axis of the computational domain ($r = 0$).

3. Modeling results and discussion

3.1. Modeling results of laminar plasma impinging-jet

Typical computed results of the temperature, axial-velocity and argon mass fraction distributions in the laminar impinging jet are shown in Fig. 3. Due to the

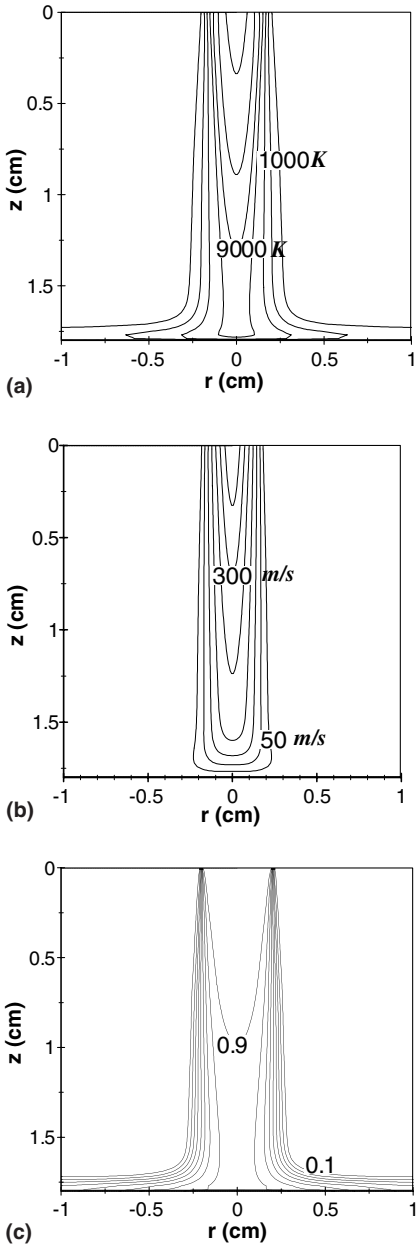

Fig. 3. Computed temperature, axial-velocity and argon mass fraction distributions in the plasma jet for the case with $T_0 = 14{,}000$ K and $U_0 = 400$ m s^{-1}. (a) Isotherms, outer line—1000 K, interval—2000 K; (b) axial velocity contours, outer line—50 m s^{-1}, interval—50 m s^{-1}; (c) argon mass fraction contours, outer line—0.1, interval—0.1.

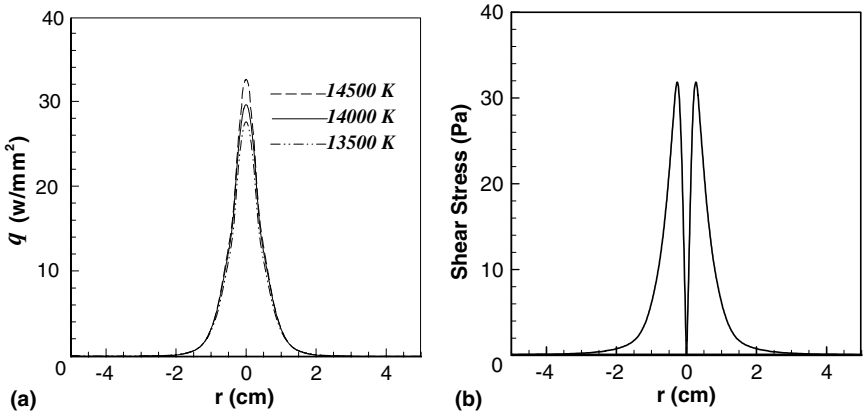

Fig. 4. Heat flux density and shear stress distributions on the workpiece surface for the case with $U_0 = 400\ \mathrm{m\ s^{-1}}$. (a) Heat flux distributions for $T_0 = 14{,}500$ K (dashed line), 14,000 K (solid line) and 13,500 K (dash-dotted line); (b) jet shear stress distribution for $T_0 = 14{,}000$ K.

continuous entrainment of the ambient air into the argon plasma jet, the plasma temperature, axial velocity and argon mass fraction decrease from 14,000 K, 400 m s^{-1} and 1.0 at the jet-inlet center to about 7000 K, 50 m s^{-1} and 0.85 at the upper edge of the stagnation-point boundary layer, respectively. The calculated heat flux density distributions on the workpiece surface for the cases with the maximum velocity $U_0 = 400\ \mathrm{m\ s^{-1}}$ and the highest temperatures $T_0 = 13{,}500$, 14,000 and 14,500 K at the plasma jet inlet are shown in Fig. 4(a). As expected, the calculated heat flux densities on the workpiece surface assume their maximum values at the jet axis and decrease rapidly in the radial direction, whereas the maximum heat flux and its half-width (width corresponding to a half of the maximum) increase with increasing jet-inlet temperature (T_0) or velocity (U_0). The predicted shear stress distribution on the workpiece surface in Fig. 4(b) for the case with $T_0 = 14{,}000$ K and $U_0 = 400\ \mathrm{m\ s^{-1}}$ shows that the calculated shear stress increases rapidly from zero at the jet center (the stagnant point, where the radial velocity component is zero) to the maximum value at $r \approx 3$ mm, and then drops rapidly with the increase of radial distance. The value and radial distance from the stagnant point of the maximum shear stresses increase with increasing jet-inlet velocity. The computed results of the heat flux and shear stress distributions on the workpiece surface are then employed as the input boundary conditions at the top surface of the workpiece in the modeling study of the workpiece re-melting process.

3.2. Modeling results of workpiece re-melting

In the workpiece re-melting modeling, carbon steel properties are used, i.e. density 7800 kg m^{-3}, thermal conductivity 40 W m^{-1} K^{-1}, viscosity 0.006 Pa s, specific heat 666 J kg^{-1} K^{-1}, melting latent-heat 2.7×10^5 J kg^{-1} and boiling point 3023 K. The solidus and liquidus temperatures of melting mushy-region are taken to be $T_S = 1523$ K and $T_L = 1723$ K, respectively, and T_L is used to represent the outer edge of the molten pool.

It is anticipated that the power absorbed by the workpiece from the impinging plasma jet is consumed to the solid-phase heating and melting, the liquid-phase heating and the surface radiation loss of the workpiece material. At first we compare the computed results for the case in which only heat conduction is considered with that in which the convection effects are also considered, including those caused by the surface tension gradient (Marangoni convection), the plasma-jet-induced shear stress on the workpiece top surface and the buoyancy force within the molten pool (natural convection). The computed results for the case with $T_0 = 13{,}500$ K are shown in Fig. 5, indicating that the convection effects may appreciably affect the molten pool shape and sizes even for this case with lower T_0 value. This fact demonstrates that only considering heat conduction is not enough for the workpiece re-melting modeling.

In order to check whether or not the modeling results is dependent on the chosen mesh, the computed isotherms on the vertical symmetrical plane (x–z plane with $y = 0$) and on the top surface (x–y plane with $z = h$, where h is workpiece thickness) using two different meshes are compared in

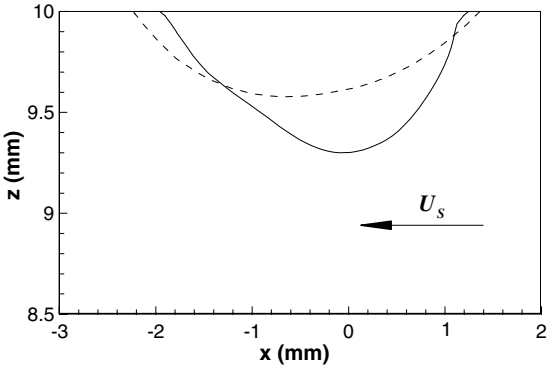

Fig. 5. Computed molten pool shapes for the case with $T_0 = 13{,}500$ K, $U_0 = 400\ \mathrm{m\ s^{-1}}$ and $U_s = 2\ \mathrm{mm\ s^{-1}}$. Solid line—with convection, $\mathrm{d}\sigma/\mathrm{d}T = -5.0 \times 10^{-4}\ \mathrm{kg\ s^{-2}\ K^{-1}}$; dashed line—without convection (pure conduction).

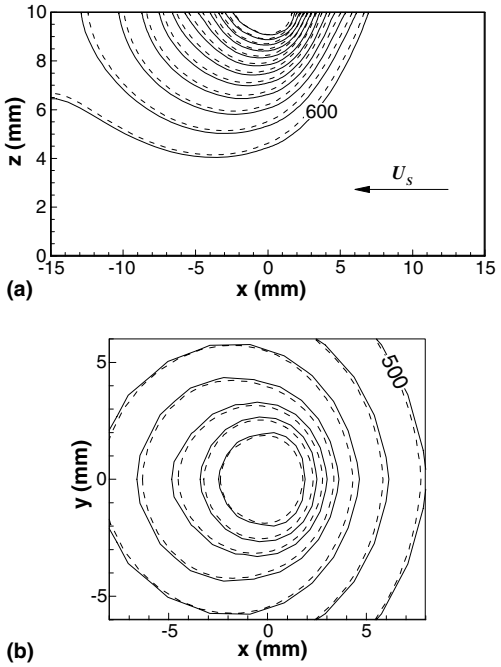

Fig. 6. Computed isotherms (a) on the vertical symmetrical plane ($y = 0$) and (b) on the top surface ($z = h$) by use of the 36 (r-) × 12 (θ-) × 36 (z-direction) mesh (solid lines) and the 48 (r-) × 22 (θ-) × 36 (z-direction) mesh (dashed lines). $T_0 = 14{,}000$ K, $U_0 = 400$ m s^{-1}, $U_s = 2$ mm s^{-1} and $d\sigma/dT = -5.0 \times 10^{-4}$ kg s^{-2} K^{-1}. Isotherm interval: 100 K for (a) and 200 K for (b). The innermost solid or dashed line represents the outer edge of the molten pool.

Fig. 6 for the case with $T_0 = 14{,}000$ K, $U_0 = 400$ m s^{-1}, the workpiece moving speed $U_s = 2$ mm s^{-1} and the temperature coefficient of melt surface tension $d\sigma/dT = -5.0 \times 10^{-4}$ kg s^{-2} K^{-1}. Solid line in this figure represent the computed results with the 36 (r-) × 12 (θ-) × 36 (z-direction) mesh, whereas dashed lines are obtained with a finer mesh, i.e. 48 (r-) × 22 (θ-) × 36 (z-direction). It is seen in Fig. 6 that almost the same predicted results are obtained, especially for the molten-pool position, shape and sizes. Hence, the 36 (r-) × 12 (θ-) × 36 (z-direction) mesh has been employed in the modeling study for other cases.

For the same case as in Fig. 6 (i.e. $T_0 = 14{,}000$ K, $U_0 = 400$ m s^{-1}, $U_s = 2$ mm s^{-1} and $d\sigma/dT = -5.0 \times 10^{-4}$ kg s^{-2} K^{-1}), Fig. 7 plots the computed velocity vector field and molten pool shape on the vertical symmetrical plane ($y = 0$). When the workpiece motion is absent, axi-symmetrical temperature and melt velocity distributions about the plasma torch/jet axis have been obtained (not shown here as separate figures), as expected. However, as seen in Figs. 6 and 7, the workpiece motion in the $-x$-direction causes the asymmetry of the computed isotherms and flow field in the x-direction even for the case with such a low workpiece moving speed of $U_s = 2$ mm s^{-1}.

3.2.1. Effects of plasma-jet heat flux

The computed molten pool shapes are compared on the vertical symmetrical plane in Fig. 8(a), on the top surface

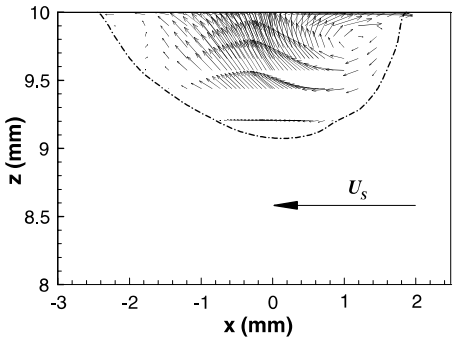

Fig. 7. Computed velocity vector field on the vertical symmetrical plane ($y = 0$). $T_0 = 14{,}000$ K, $U_0 = 400$ m s^{-1}, $U_s = 2$ mm s^{-1} and $d\sigma/dT = -5.0 \times 10^{-4}$ kg s^{-2} K^{-1}.

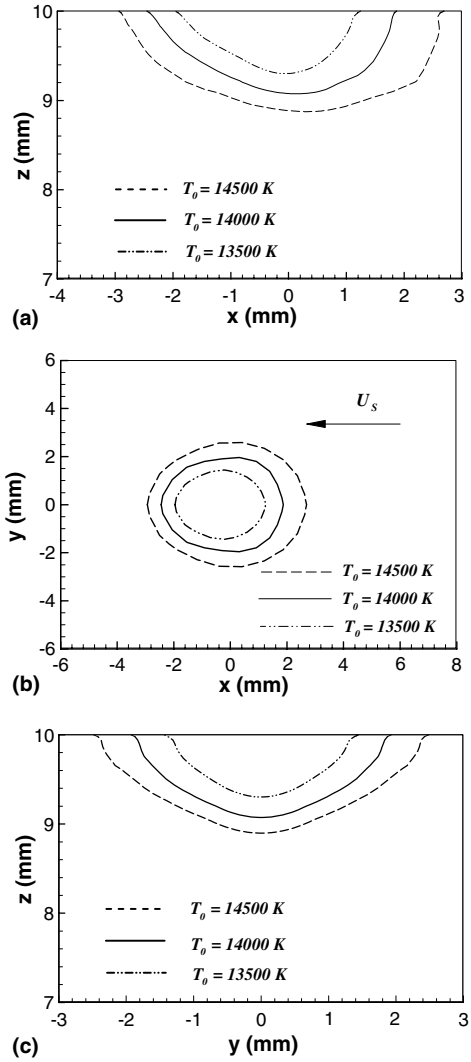

Fig. 8. Molten pool shapes for the cases with the same U_0 (400 m s^{-1}), U_s (2 mm s^{-1}) and $d\sigma/dT$ (-5.0×10^{-4} kg s^{-2} K^{-1}) but different T_0. (a) On the vertical symmetrical plane; (b) on the top surface; (c) on the y–z plane with $x = 0$. $T_0 = 14{,}500$ K (dashed line), $T_0 = 14{,}000$ K (solid line), $T_0 = 13{,}500$ K (dash-dotted line).

(x–y plane with $z = h$) in Fig. 8(b) and on the y–z plane with $x = 0$ in Fig. 8(c) for the cases with the same U_0

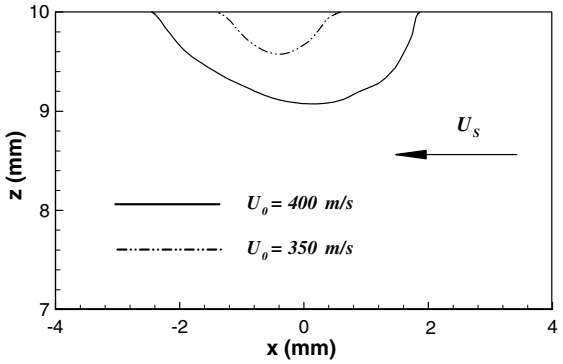

Fig. 9. Molten pool shapes on the vertical symmetrical plane for different jet velocities. $T_0 = 14{,}000$ K; $U_s = 2$ mm s^{-1}; $d\sigma/dT = -5.0 \times 10^{-4}$ kg s^{-2} K^{-1}; $U_0 = 350$ m s^{-1} (dash-dotted line) and $U_0 = 400$ m s^{-1} (solid line).

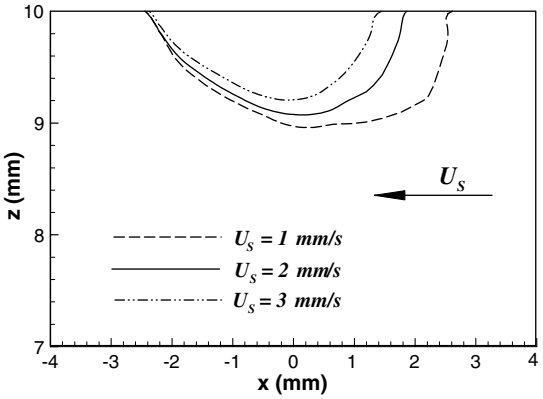

Fig. 10. Computed molten pool shapes on the vertical symmetrical plane for different workpiece speeds. $T_0 = 14{,}000$ K; $U_0 = 400$ m s^{-1}; $d\sigma/dT = -5.0 \times 10^{-4}$ kg s^{-2} K^{-1}; $U_s = 1$ mm s^{-1} (dashed line), $U_s = 2$ mm s^{-1} (solid line) and $U_s = 3$ mm s^{-1} (dash-dotted line).

(400 m s^{-1}), U_s (2 mm s^{-1}) and $d\sigma/dT$ (-5.0×10^{-4} kg s^{-2} K^{-1}) but different T_0 values ($T_0 = 13{,}500$, 14,000 and 14,500 K). Fig. 8 shows that deeper, longer and wider molten pools are obtained at higher jet-inlet temperatures (T_0). The lengths of 3.3, 4.3 and 5.5 mm, the depths of 0.7, 0.9 and 1.2 mm, and the widths of 2.9, 3.9 and 5.0 mm of the molten pools are correspondent to the cases in which $T_0 = 13{,}500$, 14,000 and 14,500 K are applied, respectively.

Fig. 9 shows the computed molten pool shapes on the vertical symmetrical plane for the cases with the same T_0 (14,000 K), U_s (2 mm s^{-1}) and $d\sigma/dT$ (-5.0×10^{-4} kg s^{-2} K^{-1}) but different U_0 values ($U_0 = 350$ and 400 m s^{-1}). It is seen from Fig. 9 that the jet-inlet velocity (U_0) also significantly affects the molten pool shapes and sizes, i.e. the molten pool becomes longer and deeper at higher U_0.

The results of Figs. 8 and 9 can be easily understood because the heat flux density from the plasma jet to the workpiece top surface increases with increasing T_0 for the given U_0 or with increasing U_0 for the given T_0.

3.2.2. Effects of workpiece moving speed

The computed molten pool shapes on vertical symmetrical plane of the workpiece are compared in Fig. 10 for the cases with the same U_0 (400 m s^{-1}), T_0 (14,000 K) and $d\sigma/dT$ (-5.0×10^{-4} kg s^{-2} K^{-1}) but different workpiece moving speed (U_s). It is seen from Fig. 10 that with the increase of U_s, shorter, shallower and more asymmetrical (with respect to the y–z plane at $x = 0$) molten pools are obtained. This prediction is reasonable, since the increase of the workpiece moving speed means that more workpiece material has to be heated by the incident heat flux. It is found that the x-locations of the rear edge of the molten pool at the top surface of the molten pool (on the left-hand side) are less influenced by the values of U_s, while the x-location of the frontal edge (on the right-hand side) appreciably shifts towards the molten pool center with increasing U_s value.

3.2.3. Effects of Marangoni convection

Because the temperature distribution on the top surface of the molten pool is non-uniform, there must exist an additional force driving the melt motion due to the existence of surface tension gradient (Marangoni convection). If the temperature coefficient of surface tension is negative ($d\sigma/dT < 0$) as for many metallic materials, the melt on the top surface of the molten pool will flow radially outwards from the molten pool center (with higher temperature) to the molten pool edge due to the driving of the surface tension gradient.

In the computation of this subsection, the T_0, U_0 and U_s are fixed to be 14,000 K, 400 m s^{-1} and 2 mm s^{-1}, respectively. Fig. 11 compares the computed molten pool shapes for different temperature coefficients of surface tension $d\sigma/dT$, and the dashed, solid and dash-dotted lines in this figure correspond to $d\sigma/dT = 0$, -1.0×10^{-4} and -1.0×10^{-3} kg s^{-2} K^{-1}, respectively. From the computed results shown in Fig. 11, it is interesting to note some special features of fluid flow and heat transfer inside the molten pool.

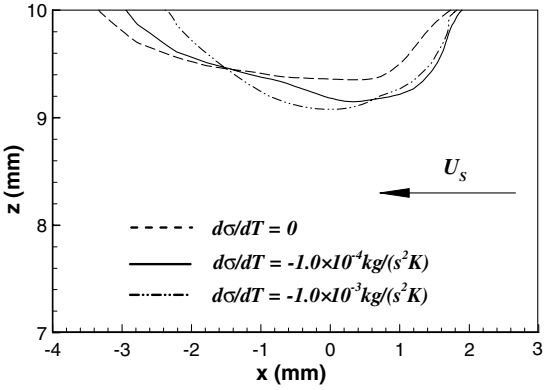

Fig. 11. Comparison of the computed molten pool shapes on the vertical symmetrical plane for the cases with $T_0 = 14{,}000$ K, $U_0 = 400$ m s^{-1}, $U_s = 2$ mm s^{-1} but different temperature coefficients of surface tension. $d\sigma/dT = 0$ (dashed line), $d\sigma/dT = -1.0 \times 10^{-4}$ kg s^{-2} K^{-1} (solid line) and $d\sigma/dT = -1.0 \times 10^{-3}$ kg s^{-2} K^{-1} (dash-dotted line).

The x-locations of the frontal edge (on the right-hand side) at the top surface of the molten pool are less influenced by the values of $d\sigma/dT$, while the x-locations of the rear edge (on the left-hand side) appreciably depend on the values of $d\sigma/dT$ (the rear edge of the molten pool at the top surface shifts towards the molten pool center with increasing absolute value of temperature coefficients of surface tension). With the increase of $|d\sigma/dT|$, the molten pool becomes somewhat shorter but deeper. It is found that with the increase of $|d\sigma/dT|$, the maximum melt velocity in the molten pool increases but the highest temperature decreases. Corresponding to $d\sigma/dT = 0$, -1.0×10^{-4} and -1.0×10^{-3} kg s^{-2} K^{-1}, the maximum melt velocities are 0.35, 0.52 and 0.73 m s^{-1}, while the highest melt temperatures are 2075, 2015 and 1860 K, respectively, in the molten pool. Since the workpiece moving speed U_s is fixed and the total power absorbed by the molten pool is almost the same for the three cases, the volumes of the molten pool would remain approximately a constant, and thus the deeper molten pool at larger $|d\sigma/dT|$ must be somewhat shorter. It is noted that the highest temperatures of the molten pool are always lower than the carbon-steel boiling point (3023 K), and thus neglecting the effect of workpiece surface vaporization on the heat flux in boundary condition (16) at the top surface of the workpiece is justified.

Sometimes, in order to change the surface property of the workpiece in actual materials processing, some trace elements such as Mg, S etc. could be put at the workpiece surface (e.g. as they are contained in a flux put on the workpiece surface [7]) and thus be added into the molten pool, resulting in a positive temperature coefficient of surface tension. Fig. 12 shows a typical computed result concerning the molten pool shape and velocity vector field on the vertical symmetrical plane ($y = 0$) for the case with $d\sigma/dT > 0$. It is clearly seen in Fig. 12 that now the melt at the top surface flows from the molten pool edge towards the center, in contrast with Fig. 7 where the melt flows with an opposite direction at the molten pool surface. In addition, comparison of the result presented in Fig. 12 to that presented in Fig. 7 shows that the molten pool for the case

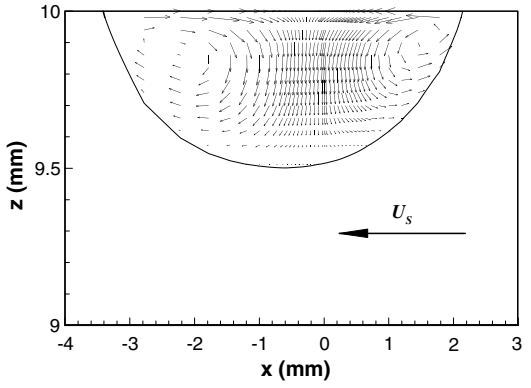

Fig. 12. Computed molten pool shape and velocity vector field on the vertical symmetrical plane for the case with $d\sigma/dT = 5.0\times10^{-4}$ kg s^{-2} K^{-1}. $T_0 = 14{,}500$ K, $U_0 = 400$ m s^{-1} and $U_s = 2$ mm s^{-1}.

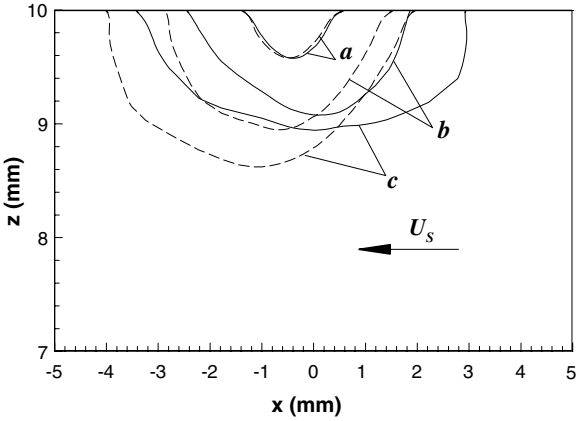

Fig. 13. Comparison of the computed molten pool shapes on the vertical symmetrical plane for the cases with (solid lines) and without (dashed lines) accounting for the jet shear stress effects. $T_0 = 14{,}000$ K, $U_s = 2$ mm s^{-1} and $d\sigma/dT = -5.0\times10^{-4}$ kg s^{-2} K^{-1}. (a) $U_0 = 350$ m s^{-1}; (b) $U_0 = 400$ m s^{-1}; and (c) $U_0 = 450$ m s^{-1}.

with $d\sigma/dT > 0$ is somewhat longer but shallower than that for the case with $d\sigma/dT < 0$.

3.2.4. Effects of the jet shear stress

In the laminar plasma-jet re-melting processing of metal surface, the shear stress caused by the impinging plasma jet at the workpiece surface may affect the melt flow and the molten-pool shape. Fig. 13 shows the computed molten pool shapes for the cases with the same T_0 (14,000 K), U_s (2 mm s^{-1}) and $d\sigma/dT$ (-5.0×10^{-4} kg s^{-2} K^{-1}), but different U_0, i.e. $U_0 = 350$ m s^{-1} (a), $U_0 = 400$ m s^{-1} (b) and $U_0 = 450$ m s^{-1} (c). The solid lines represent the cases with accounting for the jet shear stress, while dashed lines without accounting for the jet shear stress. Fig. 13 suggests that the jet shear stress may appreciably affect the molten pool shape, location and sizes, and this effect can be ignored only at lower jet-inlet velocities (e.g. for $U_0 = 350$ m s^{-1} or lower).

3.2.5. Effects of natural convection

Another factor that may affect the melt flow within the molten pool is the natural convection due to the non-uniform temperature distribution within the molten pool. Typical computed results demonstrate that the natural convection effect can be safely neglected (not shown here as a separate figure) since the depth of molten pool is usually small.

3.2.6. Discussion about the employment of boundary conditions

It is expected that the impact pressure of the impinging plasma jet may cause the depression of the top surface of molten-pool. So far there is no direct observed result about the molten-pool surface deformation for the plasma re-melting processing. However, experimental and modeling results [17,18] show that the effect of the surface deformation on the molten-pool is negligible even for the arc

welding (with higher impact pressure) provided that the arc current is less than 200 A. It is believed that employing the flat top surface assumption in this paper (as in many previous studies [5–8]) can reveal the main features of the heat transfer and fluid flow in the laminar-plasma material re-melting processing, especially for the molten-pool shape and sizes in which we are most interested. Considering the deformation of top molten-pool surface will require using a body-fitted coordinate system [18] and solving an additional equation about the melt-gas interface form, and thus require much more numerical efforts. This complicated factor is remained as the subject of subsequent studies.

Zero temperature gradient in the x-direction has been used as the downstream boundary condition of the computational domain. This treatment is reasonable for the case with higher workpiece moving-speed (U_s). When the workpiece moving-speed is comparatively low, the zero temperature gradient condition will cause inaccuracy of the temperature field near the downstream boundary. However, the calculated position, shape and sizes of the molten-pool are less influenced by the downstream and lateral boundary conditions.

The isothermal boundary condition has been employed at the bottom boundary of the workpiece for solving the energy equation. It is expected that this is reasonable choice when the workpiece is put on a metallic working platform. Modeling results show that changing to employ an insulated condition at the bottom boundary less influences the predicted shape and sizes of the molten pool, although the temperature distribution near the bottom boundary is somewhat different.

3.2.7. Comparison of modeling results with experimental observation

Although so far no other theoretical predictions can be used to compare with the present predicted results, we can compare our modeling results with some available experimental observation. The laminar plasma torch and its operating conditions used in the experimental study of Pan et al. [3] are similar to those employed in this modeling study. In their experiment, the laminar DC non-transferred arc plasma jet was used to heat the cast iron for re-melting hardening. The distance from the torch nozzle exit to the workpiece surface is 9 mm, the workpiece moving speed 0.5–5 mm s^{-1}, the argon flow rate in the range of 75–220 STP cm^3 s^{-1} and the arc current varies in the range of 180–195 A. It was found that the re-melting trace width and the hardening layer depth increase with increasing arc current (or increasing plasma jet-inlet temperature and velocity), in consistence with the present modeling results. The molten pool widths observed in their experiment were in the range of 2.0–4.0 mm, whereas the thickness of the hardened layer was the range of 0.6–1.7 mm corresponding to the molten-pool depths of 0–1.1 mm (obtained by subtracting the estimated thickness ~0.6 mm of the solid-phase transfer hardening layer from the thickness of the whole hardened layer [3]). These experimental results also agree reasonably with the present modeling results.

4. Conclusions

Modeling study has been performed concerning the heat transfer and fluid flow in the carbon steel re-melting by the laminar argon plasma jet impinging normally upon the workpiece located in air surroundings. The results show that the jet-inlet temperature and velocity, workpiece moving speed and Marangoni convection affect significantly the heat transfer and fluid flow in the molten pool and thus affect its shape and sizes. The effects of the shear stress caused by the impinging plasma jet are important only at higher jet-inlet velocities. The effects of natural convection can be ignored. The predicted results are reasonably consistent with available experimental data.

Acknowledgements

This study was supported by the National Natural Science Foundation of China (Nos. 50336010, 50276065 and 10405015) and the Chinese Postdoctoral Science Foundation (No. 20040350044).

References

[1] W.X. Pan, W. Hua Zhang, W. Hong Zhang, C.K. Wu, Generation of long, laminar plasma jets at atmospheric pressure and effects of flow turbulence, Plasma Chem. Plasma Process. 21 (1) (2001) 23–35.
[2] W.X. Pan, W.H. Zhang, W. Ma, C.K. Wu, Characteristics of argon laminar DC plasma jet at atmospheric pressure, Plasma Chem. Plasma Process. 22 (2) (2002) 271–283.
[3] W.X. Pan, X. Meng, G. Li, Q.X. Fei, C.K. Wu, Feasibility of laminar plasma-jet hardening of cast iron surface, Surf. Coat. Technol. 197 (2005) 345–350.
[4] W.X. Pan, W. Ma, C.K. Wu, Surface materials processing with DC laminar plasma jets, in: Y.C. Zhou, Y.X. Gu, Z. Li (Eds.), Mechanics and Material Engineering for Science and Experiments, Science Press, Beijing, 2001, pp. 427–431.
[5] A.P. Mackwood, R.C. Crafer, Thermal modelling of laser welding and related processes: a literature review, Opt. Laser Technol. 37 (2005) 99–115.
[6] M. Tanaka, M. Ushio, J.J. Lowke, Numerical study of gas tungsten arc plasma with anode melting, Vacuum 73 (2004) 381–389.
[7] J.J. Lowke, M. Tanaka, M. Ushio, Mechanisms giving increased weld depth due to a flux, J. Phys. D: Appl. Phys. 38 (18) (2005) 3438–3445.
[8] X.H. Ye, X. Chen, Three-dimensional modelling of heat transfer and fluid flow in laser full-penetration welding, J. Phys. D: Appl. Phys. 35 (10) (2002) 1049–1056.
[9] A.B. Murphy, Diffusion in equilibrium mixtures of ionized gases, Phys. Rev. E 48 (5) (1993) 3594–3603.
[10] A.B. Murphy, Transport coefficients of air, argon–air, nitrogen–air, and oxygen–air plasmas, Plasma Chem. Plasma Process. 15 (2) (1995) 279–307.
[11] D.Y. Xu, X. Chen, K. Cheng, Three-dimensional modelling of the characteristics of long laminar plasma jets with lateral injection of carrier gas and particulate matter, J. Phys. D: Appl. Phys. 36 (13) (2003) 1583–1594.
[12] K. Cheng, X. Chen, Effects of natural convection on the characteristics of long laminar argon plasma jets issuing upwards or downwards into ambient air—a numerical study, J. Phys. D: Appl. Phys. 37 (17) (2004) 2385–2391.

[13] K. Cheng, X. Chen, W.X. Pan, Comparison of laminar and turbulent thermal plasma jet characteristics—a modeling study, Plasma Chem. Plasma Process., in press.
[14] V.R. Voller, C.R. Swaminathan, B.G. Thomas, Fixed grid techniques for phase change problems: a review, Int. J. Numer. Methods Eng. 30 (1990) 875–898.
[15] S.V. Patankar, Numerical Heat Transfer and Fluid Flow, McGraw-Hill, New York, 1980.
[16] J. Zhu, An introduction and guide to the computer program FAST-3D, Institute for Hydromechanics, University of Karlsruhe, Report No. 691, 1992.
[17] M.L. Lin, T.W. Eagar, Influence of arc pressure on weld pool geometry, Weld. J. 64 (6) (1985) 163s–169s.
[18] S.-D. Kim, S.-J. Na, Effect of weld pool deformation on weld penetration in stationary gas tungsten arc welding, Weld. J. 71 (5) (1992) 179s–200s.